



HAL
open science

Hydrodynamics in a stirred tank in the transitional flow regime

Freyman Mendoza, A. Lopes Bañales, Emmanuel Cid, Catherine Xuereb, Martine Poux, David F. Fletcher, Joelle Aubin

► **To cite this version:**

Freyman Mendoza, A. Lopes Bañales, Emmanuel Cid, Catherine Xuereb, Martine Poux, et al.. Hydrodynamics in a stirred tank in the transitional flow regime. *Chemical Engineering Research and Design*, 2018, 132, pp.865-880. 10.1016/j.cherd.2017.12.011 . hal-01982666

HAL Id: hal-01982666

<https://hal.science/hal-01982666>

Submitted on 15 Jan 2019

HAL is a multi-disciplinary open access archive for the deposit and dissemination of scientific research documents, whether they are published or not. The documents may come from teaching and research institutions in France or abroad, or from public or private research centers.

L'archive ouverte pluridisciplinaire **HAL**, est destinée au dépôt et à la diffusion de documents scientifiques de niveau recherche, publiés ou non, émanant des établissements d'enseignement et de recherche français ou étrangers, des laboratoires publics ou privés.



Open Archive Toulouse Archive Ouverte (OATAO)

OATAO is an open access repository that collects the work of Toulouse researchers and makes it freely available over the web where possible

This is an author's version published in: <http://oatao.univ-toulouse.fr/21125>

Official URL: <https://doi.org/10.1016/j.cherd.2017.12.011>

To cite this version:

Mendoza, Freyman  and Bañales, A. Lopes  and Cid, Emmanuel  and Xuereb, Catherine  and Poux, Martine  and Fletcher, David F. and Aubin, Joelle 
Hydrodynamics in a stirred tank in the transitional flow regime. (2018) Chemical Engineering Research and Design, 132. 865-880. ISSN 0263-8762

Any correspondence concerning this service should be sent to the repository administrator: tech-oatao@listes-diff.inp-toulouse.fr

Hydrodynamics in a stirred tank in the transitional flow regime

F. Mendoza^a, A. Lopes Bañales^a, E. Cid^a, C. Xuereb^a, M. Poux^a,
D.F. Fletcher^b, J. Aubin^{a,*}

^a Laboratoire de Génie Chimique, Université de Toulouse, CNRS, INPT, UPS, France

^b School of Chemical and Biomolecular Engineering, The University of Sydney, Australia

ARTICLE INFO

Keywords:

Mixing

Stirred tank

Transitional flow regime

CFD

PIV

Macro-instabilities

ABSTRACT

The hydrodynamics in a stirred tank in the transitional flow regime have been studied experimentally and numerically with data obtained by Particle Image Velocimetry and Computational Fluid Dynamics, respectively, at three Reynolds numbers, $Re = 340, 980$ and 3000 . The effects of impeller rotation speed and fluid properties on the underlying flow structures have been investigated. Data are analysed by mean flow fields, as well as with Proper Orthogonal Decomposition, which gives an insight into the flow dynamics by separating the spatial and temporal characteristics of the flow structures. Experimentally, it has been found that dimensionless velocity fields depend on fluid properties and impeller speed at $Re = 340$ and 980 , whilst they are self-similar at $Re = 3000$. Coherent flow structures only exist however at $Re = 340$ and the flow is structurally different than that at higher Re . Characteristic frequencies identified for $Re = 980$ and 3000 are $0.03N$ and $0.13N$, which are consistent with previous work in the literature. The simulations conducted at $Re = 340$ are in reasonable agreement with the experimental data, however, they do not predict a dependency of flow characteristics on fluid properties and impeller speed. This inconsistency is attributed to the difficulty of performing experiments that are free of physical perturbations, which may have a significant effect on flows at low transitional Reynolds numbers.

1. Introduction

Whilst much research in the past two decades has focused on process intensification and new technologies for continuous processing, which demonstrate numerous advantages, traditional batch stirred tanks are still largely present in the process industries. Indeed, the replacement of existing batch processes with continuous flow technologies is not systematic mainly because companies do not want to, or cannot, reinvest in new equipment and process expertise, regardless if there could be significant gains in terms of product quality, productivity, safety and/or environmental impact. As a result, industry is still seeking to improve their understanding and engineering knowledge of existing batch processes and particularly how the process can be operated in order to control product quality, as well as to manage possible downstream processing steps, energy and waste.

Amongst the numerous batch stirred tank processes present in a broad range of sectors, including chemicals, agrochemicals, pharmaceuticals, cosmetics, food and mining, operation in the transitional flow regime is very frequent. This is mainly because in stirred tanks the laminar flow regime is limited to very low impeller Reynolds numbers (Re), typically $Re < 10-100$, the onset of flow instabilities occurring earlier than in tubes due to the rotating impeller and interaction with the vessel geometry. The fully-developed turbulent flow regime is typically considered when $Re \geq 20\,000$, although studies have shown that a $Re \geq 300\,000$ is often required in order to obtain fully turbulent flow in both the recirculation zone and the top third of the tank (Machado et al., 2013). Despite this, a large majority of studies presented in the literature dating back to the 1950s focus on full-developed turbulent flows or purely laminar flows. This is because flow instabilities and the lack of scaling of transitional flows make experiments and simulations

* Corresponding author.

E-mail address: joelle.aubincano@ensiacet.fr (J. Aubin).

<https://doi.org/10.1016/j.cherd.2017.12.011>

difficult. As a result, engineering design rules and recommendations for stirred tank applications are typically valid for turbulent or laminar flows only.

The few studies in the literature dealing with the transitional flow regime in stirred tanks address specific particularities of these flows; however, determination of the general underlying reasons for physical phenomena occurring is not generally the focus. For example, [Machado and Kresta \(2013\)](#) and [Machado et al. \(2013\)](#) studied the transition from turbulent to transitional flow in various stirred tank geometries in order to determine the limits of fully turbulent scaling in different zones of the tank. They showed that although fully-developed turbulent flow is generally considered for $Re > 20\,000$ in standard stirred tank geometries, this is only true close to the impeller. Reynolds numbers greater than $300\,000$ are required in order to attain fully-developed turbulence at heights in the tank greater than $0.9T$. However, in non-conventional geometries like the confined impeller stirred tank (CIST), fully turbulent flow was observed at Reynolds numbers as low as 3000 . More generally, it was found that fully turbulent flow occurs at lower Reynolds numbers as the scale of the tank decreased and the ratio of impeller-to tank diameter D/T increased. They also showed that dimensionless velocity profiles at a fixed Reynolds number can depend on the viscosity of the Newtonian fluid, therefore affecting the flow regime in the tank. [Liné et al. \(2013\)](#) analysed the flow and the dissipation rate of a shear-thinning liquid in the vicinity of a Rushton turbine. Due to the rheology of the fluid, the flow was expected to be in the transitional flow regime with an impeller Reynolds of 530 , determined using the Metzner–Otto correlation. However, the validity of this method and the spatial variation of the flow regime in the tank was not discussed. Recently, [Alberini et al. \(2017\)](#) have performed 3-dimensional Particle Tracking Velocimetry (PTV) measurements in a stirred tank in transitional flow at $Re = 70$ and 1000 with the objective of comparing the measurement technique with 2-dimensional 2-component Particle Image Velocimetry (PIV) for Newtonian and non-Newtonian flows. Although the work does not focus on the characteristics of transitional flow, the authors note a slight difference in the PTV and PIV velocity fields in the impeller discharge with non-Newtonian flow. This is attributed to the unstable nature of transitional flow and suggests that the tangential velocity component may be of significance in such flows.

Other studies have been dedicated to macro-instability phenomena occurring in stirred tanks in different flow regimes. [Bruha et al. \(1996\)](#) used a tornadometer to determine the frequency of macro-instabilities (MI) as a function of Reynolds number for the range 210 – $67\,000$. No instabilities were observed when $Re = 200$, whilst a more or less constant frequency of $0.04N$ – $0.05N$ was found for $Re > 9000$. For intermediate Re , however frequencies were found to increase logarithmically with Re but no physical interpretation of the phenomena was provided. On the other hand, the same group of authors later reported a frequency of $0.087N$ at $Re = 750$ and 1200 obtained with Laser Doppler Velocimetry (LDV) measurements ([Montes et al., 1997](#)). [Galletti et al. \(2004\)](#) further studied the effects of fluid properties, operating conditions, as well as impeller and tank geometry on the frequencies of MI occurring from precessional vortex motion for Reynolds numbers ranging from 400 to $54\,400$. They made point measurements of the fluid velocity close to the free liquid surface using LDV and found that for $400 < Re < 6300$ the MI are characterised by a frequency of $0.106N$, whilst in the range $13\,600 < Re < 54\,400$, the frequency of $0.015N$ was dominant. In the intermediate range, however, both frequencies were present. They also found in general that at constant Re , a change in fluid properties did not affect the characteristic frequency, although their results do show some dispersion at the lowest Reynolds numbers studied. Later, [Ducci and Yianneskis \(2007\)](#) and [Ducci et al. \(2008\)](#) focussed on the physical mechanisms underlying the precessional vortex and associated frequencies. They conducted 2-dimensional velocity measurements on a horizontal plane under a Rushton turbine in the transitional regime $4400 < Re < 8000$ and in turbulent flow, $Re = 27200$ and analysed the data using Proper Orthogonal Decomposition (POD). They found that there are two mechanisms responsible for the MI vortex. One is a perturbation that causes the vortex to move off-centre and is related to characteristic frequencies of $0.02N$. The other is the elongation of the vortex core, which is characterised by a frequency of $0.1N$.

Their results show that the frequency $0.02N$ is associated with flows where $Re > 6000$. From the ensemble of these results, there appears to be some clear trends on the formation and characteristics of vortex macro-instabilities at high transitional Reynolds numbers, i.e. $Re > 4000$ and valid mechanisms for the behaviour of the MI have been proposed. In the lower range of transitional Reynolds numbers, however, the conclusions are less explicit.

The simulation of transitional flows in stirred tanks is challenging because hydrodynamic instabilities create unsteady flow, which needs to be correctly captured. Turbulence models are typically not well adapted at transitional flow Reynolds numbers because the eddy viscosity hypothesis used in the models is designed for high Reynolds number turbulence and also because the wall functions assume a log law at the wall. Ultimately, the full resolution of the time-dependent Navier–Stokes equations on an extremely fine 3-dimensional mesh would be desirable however such simulations require excessive computing efforts, which may not be viable for practical engineering applications. As a result, there are very few studies in the literature that deal with the simulation of transitional flow in stirred tanks and almost all of the available literature may be attributed to a single author ([Derksen, 2011, 2012a, 2012b, 2013; Zhang et al., 2017](#)). In his studies, Derksen has used the Lattice Boltzmann method to perform direct numerical simulations (DNS) of flows with Reynolds numbers in the range 2000 – 12000 . These are extremely intensive computations, which require around 100 impeller revolutions on a highly-refined grid. Although these studies do not focus particularly on the underlying nature of the transitional flow, but rather specific mixing applications, the results demonstrate that moderate Reynolds numbers allow the flow to be simulated directly, without the use of a turbulence closure or subgrid-scale models. Although, in their recent study, [Zhang et al. \(2017\)](#) have shown that even for simple Newtonian flows, DNS failed to correctly predict the flow patterns and velocity fluctuation levels at certain transitional Reynolds numbers. Their work also shows the current state of confusion in modeling transitional flows as they attempted to apply transition models developed for external aerodynamics to internal flow and performed finite volume simulations using 2nd order upwind differencing that they erroneously called finite volume DNS. The limits and capacities of simulation techniques (e.g. CFD, Lattice Boltzmann) for transitional flows in stirred tanks are therefore not clearly identified. Moreover, as various authors have discussed, the flow regime in a stirred vessel is rarely constant in the entire volume ([Ducci et al. 2008; Machado et al. 2013](#)); in some cases, flow may be fully turbulent in the vicinity of the impeller but in the transitional or even laminar flow regime in zones further away. It is not straightforward to know how this variation in flow regime should be taken into account in simulations that can be performed with reasonable computational effort and therefore applicable for engineering applications.

The global objective of this work is to contribute the knowledge of transitional flows in stirred tanks in order to develop engineering guidelines and tools that will ultimately lead to increased process/product understanding and improved product development and manufacturing. In particular, this study aims at exploring the effects of Newtonian fluid properties (viscosity, density) and impeller rotation speed on the characteristics of transitional flow experimentally via PIV measurements and numerically with transient laminar flow CFD simulations. The flow is examined using conventional mean flow analysis and the in more detail with POD.

2. Materials and methods

2.1. Stirred tank geometry

The tank geometry employed in this work is a dish-bottomed cylindrical tank, $T = H = 0.19$ m, with four equally spaced Perspex baffles of width $w = T/10$ placed 90° to each other. The cylindrical vessel is placed inside a square tank whose front panel is transparent to allow distortion-free velocity measurements. The tank was filled with plain water and is

Table 1 – Operating conditions for the different cases investigated.

| Re | %wt Glycerol | Temperature (°C) | ρ (kg m ⁻³) | μ (mPa s) | N (rpm) |
|-------|--------------|------------------|------------------------------|---------------|---------|
| 340 | 90 | 30 | 1216 | 107 | 177 |
| 340 | 100 | 35 | 1252 | 247 | 400 |
| 980 | 80 | 35 | 1208 | 34 | 190 |
| 980 | 90 | 35 | 1214 | 82 | 400 |
| 3 000 | 70 | 35 | 1187 | 19 | 296 |
| 3 000 | 80 | 40 | 1204 | 29 | 444 |

connected to a pump and a heating element in order to heat the working fluid in the cylindrical tank to a specific temperature. The cylindrical tank is equipped with a down-pumping Lightnin A320 axial flow impeller ($D=T/2$), which is a wide-bladed hydrofoil impeller that is recommended for higher viscosity applications and low Reynolds number. The impeller is mounted on a shaft, $s=0.008$ m, which extends to the bottom of the vessel. The impeller clearance is $C=T/3$, where C is defined as the distance from the vessel bottom to the lowest horizontal plane swept by the impeller.

2.2. Operating conditions

The operating conditions were chosen to obtain two experimental datasets for three different Reynolds numbers equal to 340, 980 and 3000. To do this both the fluid viscosity, μ , and the impeller speed, N , were varied. To vary the fluid viscosity different concentrations of aqueous glycerol solutions were used at different temperatures. Temperature controlled viscosity measurements were made with an AR 2000 rheometer (TA Instruments); density was measured with a DMA 38 densimeter (Anton Paar) where temperature is controlled with a Peltier resistance. Care was taken to keep the axial impeller tip speed (πND) in the recommended range of 1–5 m s⁻¹. Table 1 shows the operating conditions for the six different cases studied.

2.3. Particle image velocity measurements

Full field 2-dimensional, 2-component velocity measurements encompassing almost the entire height of the tank (except for in the dish-bottom) were performed using PIV. The PIV was composed of a double pulsed Nd:YAG laser (532 nm, 2 × 120 mJ, Nanopiv – Litron Lasers). The liquid was seeded using rhodamine-doped polymer particles ($d_p = 10\text{--}30$ μm) (microParticles GmbH, Germany). A black and white CCD camera (ImagerProPlus) with a resolution of 4032 × 2688 pixels² and a high-pass filter was used to record instantaneous images of the flow in a plane midway between two baffles. Image pairs were taken at a rate of 9 Hz and for each case 1000 instantaneous velocity fields were recorded. These images were processed using DaVis software (LaVision, Germany). A decreasing interrogation window size (from 64 × 64 pixels² to 32 × 32 pixels²) with 50% overlap and the standard cross-correlation with Fast Fourier Transform (FFT) was used to determine the corresponding spatially averaged displacement vectors. The spatial resolution was 1.5 mm.

2.4. CFD simulations

Transient, laminar flow simulations for both cases at Re = 340 were made using the commercial CFD software ANSYS CFX (V18.1). A CAD model of the A320 impeller supplied by SPXFLOW was de-featured and incorporated into a model

of the vessel using ANSYS SpaceClaim. A tetrahedral mesh, with 5 layers of inflation at the walls, was then created with three different mesh densities, comprising 1.01, 2.07 and 6.46 million cells. All presented simulation results used the finest mesh (see later for details). The equations were solved using the coupled solver with High Resolution differencing for the convective terms and the Second Order Backward Euler scheme for the time derivatives. The solution at any time-step was deemed to have converged when the normalised RMS residuals fell below 10⁻⁵.

Initially a steady-state simulation was run using the Frozen Rotor model, which assumes fixed relative position of the blades and baffles, to generate a starting flow and to study mesh dependency. Following this, transient simulations were run using the moving mesh approach with the Transient Rotor Stator interface model and a 2° displacement of the blades per time-step. Simulations were continued for over 200 revolutions of the impeller in both cases. At these times, quasi-periodic behaviour of the torque on the blades was observed. Data generated only after the quasi-periodic behaviour was established were used in the flow analysis. Velocity data were output on a vertical plane midway between the baffles every 0.022 s (45 Hz sampling frequency), which is 5 times that used in the experiments (9 Hz). The high sampling frequency allows numerical data to be analysed at either 9 Hz or 45 Hz, thereby allowing the effect of the sampling frequency on the results to be studied. In both cases, however, the number of data fields used for the analysis spans 62 impeller revolutions, which is much longer than the period of the flow structures being detected.

2.4.1. Computational setup and mesh

The geometry together with the location of the rotating zone (grey) and the sampling plane (red) are shown in Fig 1(a). The vertical sampling plane is positioned midway between two baffles and extends from the shaft to the tank wall. This figure also shows the computational mesh on the impeller for the 6.46 million element mesh. The top of the vessel (green) coincides with the mean liquid level, which was assumed to be flat, and a no stress boundary condition was applied. A cross-section of the 6.46 million element mesh in the entire tank is given Fig 1(b).

As mentioned above, steady-state Frozen Rotor simulations were run on three different mesh densities. In order to access mesh dependency effects, the velocity magnitude was extracted on a horizontal line from the tank centre to the wall at three-quarters height and compared for the three mesh densities. The results, given in Fig 2, show that there is a significant difference between the coarse and medium meshes but only a small difference when the medium and fine meshes are compared. Given the simulation times were acceptable, typically taking 40 min per revolution on 24 cores, all simulations used the finest mesh.

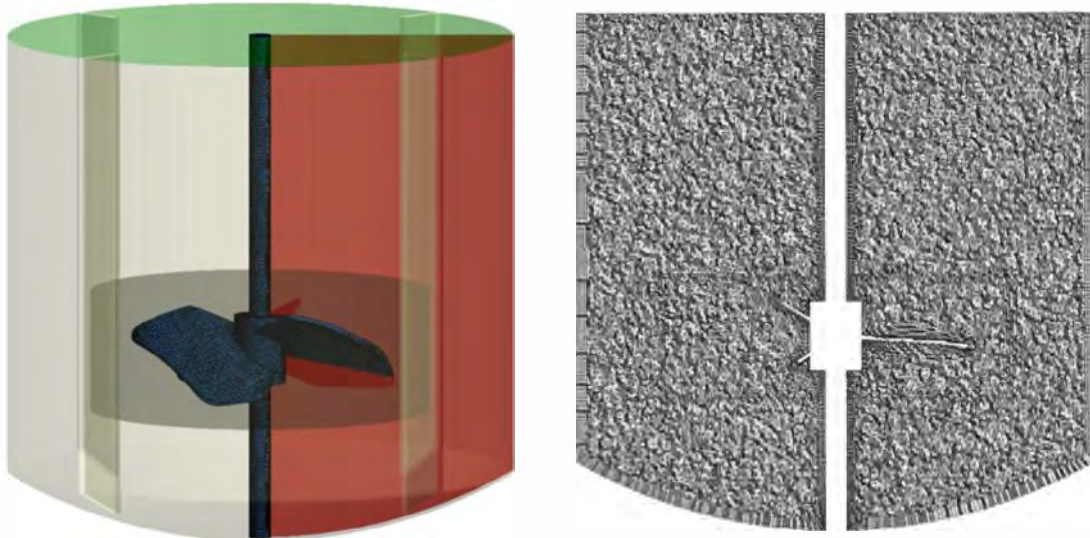


Fig. 1 – Geometry (a) and mesh (b) used in the simulations of the fully baffled dish-bottomed tank with A320 impeller. (For interpretation of the references to colour in the text, the reader is referred to the web version of this article.)

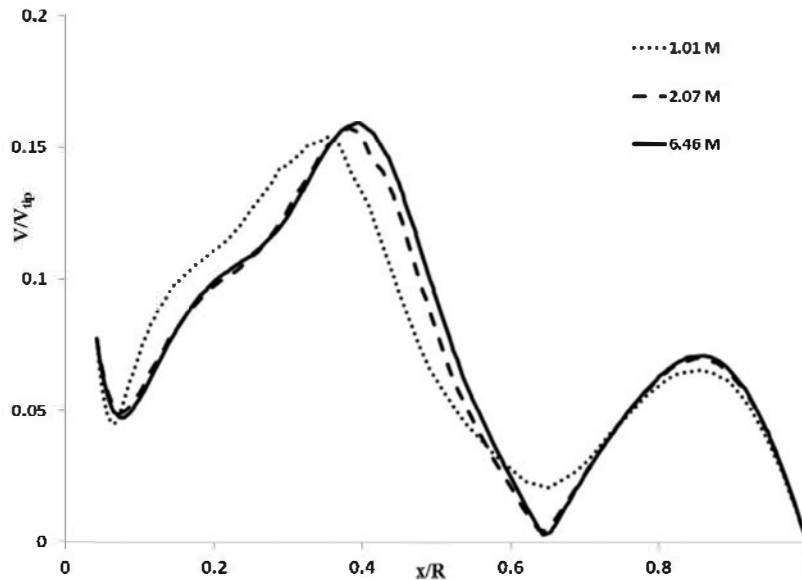


Fig. 2 – Normalized velocity magnitude on a horizontal line located on the sampling plane at three quarters of the vessel height.

2.5. Proper Orthogonal Decomposition technique

Proper Orthogonal Decomposition (also known as Karhunen–Loève decomposition in signal processing and principal component analysis in statistics) is a data processing technique, which enables large amounts of high-dimensional data to be transformed into simpler, lower-dimensional data sets that capture the key phenomena. In fluid mechanics, POD is known to be an efficient tool for isolating coherent structures from a series of instantaneous velocity fields in complex flows, as well as understanding their dynamics and predicting their temporal evolution (Holmes et al. 1997).

POD is a linear procedure, which decomposes a set of instantaneous velocity fields into a modal base, thereby allowing organized motion to be distinguished from turbulent motion (Berkooz et al., 1993). The different modes are ordered in terms of their contribution to the total kinetic energy in the plane of measurement, with the first mode being the most energetic and the last the least energetic. In this work, POD is implemented via the ‘snapshot method’ and is used to identify

coherent structures in the flow and to characterize the sensitivity of the flow structures to changes in fluid properties and operating conditions.

2.5.1. Snapshot method

In this section, a brief description of the snapshot method is given; for a more detailed description, the reader is referred to the founding works of Sirovich (1987) and Berkooz et al. (1993). The reader is also referred to the works of Liné et al. 2013 and Ducci et al. 2008 for the specific mathematical details of the snapshot method applied to PIV data. In this work, n instantaneous velocity fields in the X–Z plane are obtained by either PIV and CFD and each instantaneous velocity field measurement constitutes a snapshot of the flow dynamics.

Eq. (1) describes the POD analysis applied to the fluctuating part of a measured velocity field, where \vec{V}_k and \vec{V}_{mean} are the total and mean velocity flow fields, respectively. For each mode I , the POD method generates $\tilde{\varphi}^{(I)}$ and $a_k^{(I)}$.

The variable $\tilde{\varphi}^{(I)}$ is the spatial eigenfunction of mode I and is independent of time, or the instantaneous event, k . The vari-

able $a_k^{(l)}$ is the instantaneous temporal coefficient of mode l that is spatially independent; it also controls the importance of the eigenfunctions and the way they contribute in time to the total flow.

$$\tilde{\mathbf{V}}_k(x, y, z, t) = \tilde{\mathbf{V}}_{\text{mean}}(x, y, z, t) + \sum_{l=1}^n a_k^{(l)}(t) \tilde{\varphi}^{(l)}(x, y, z) \quad (1)$$

The spatial eigenfunctions $\tilde{\varphi}^{(l)}$ are orthogonal to each other while the temporal coefficients $a_k^{(l)}(t)$ are uncorrelated in time. The spatial eigenfunctions are obtained from the eigenmodes of the two-point correlation tensor, \mathbf{C} , as given in Eq. (2).

$$\mathbf{C} \tilde{\varphi}^{(l)} = \lambda^{(l)} \tilde{\varphi}^{(l)} \quad (2)$$

where $\lambda^{(l)}$ is the eigenvalue, which represents the energy content associated with eigenfunction $\tilde{\varphi}^{(l)}$ and its contribution to the total kinetic energy. The correlation tensor, or auto-covariance tensor, is given by Eq. (3).

$$\mathbf{C} = \overline{\tilde{\mathbf{V}}_i(x, y, z, t) \cdot \tilde{\mathbf{V}}_j(x, y, z, t)} \quad (3)$$

where the indices i and j refer to different points in the grid of measurements. It is worth noticing that numerically the auto-covariance tensor can also be given by Eq. (4).

$$\mathbf{C} = \frac{1}{N} \mathbf{M} \cdot \mathbf{M}^T = \begin{bmatrix} \overline{u^2(x_1, z_1)} & & \\ & \dots & \\ & & \overline{w^2(x_L, z_C)} \end{bmatrix} \quad (4)$$

where \mathbf{M} is the snapshot matrix, which is composed of the entire data set of instantaneous velocity fields. Each instantaneous velocity field is disposed in the matrix as a column vector, with the axial component u_1 and the radial component w_1 of velocity in the same matrix column, followed by the next instantaneous velocity field in the next column and so on for n snapshots, as shown in Eq. (5).

$$\mathbf{M} = \begin{bmatrix} u_1 & \dots & u_n \\ w_1 & \dots & w_n \end{bmatrix} \quad (5)$$

Finally, the POD coefficients $a_k^{(l)}(t)$ are obtained by projecting each instantaneous velocity field on the l -th eigenfunction, $\tilde{\varphi}^{(l)}$ as given in Eq. (6).

$$a_k^{(l)}(t) = \tilde{\mathbf{V}}_k \cdot \tilde{\varphi}^{(l)} \quad (6)$$

3. Results and discussion

3.1. Experimental data

3.1.1. Mean flow

For each Reynolds number, the mean velocity field is calculated as the time average of the entire dataset, which is composed of $n=1000$ instantaneous velocity fields. The velocity components are normalized by the tip speed of the impeller, V_{tip} . Normalised axial velocity component profiles are also plotted at three different heights in the tank: $h=0.29H$, immediately below the impeller swept plane; $h=0.5H$, mid-height of the tank; $h=0.75H$ in the upper part of the tank.

Figs. 3–5 show the mean velocity fields for two different sets of operating conditions at $Re=340$, 980 and 3 000, respectively.

The line between $y/H=0$ and $y/H=0.2$ depicts the dished bottom of the tank where no measurements were taken. These figures show the presence of a single circulation loop in the lower half of the tank that is characteristic of an axial flow impeller. In a general manner, as the Reynolds decreases the size of the circulations decreases and the jet expelled from the impeller-swept volume has an increasingly important radial flow component to it. This is expected behaviour as it is well known that the pumping capacity of axial flow impellers decreases as the flow becomes laminar (Hemrajani and Tatterson, 2004).

Comparing Fig. 3(a) and (b), it can be seen that the circulation loop is slightly smaller with the lower values of fluid viscosity and impeller speed, but the maximum relative velocity is slightly higher. Indeed, the normalised axial velocity component profiles taken at different heights in the tank, shown in Fig. 3(c), do not collapse (particularly close to the impeller swept zone), which is usually the case for highly laminar and fully-developed turbulent flow. In the upper part of the tank, the fluid velocity is close to zero. When the Reynolds number is increased to 980, as shown in Fig. 4, the flow patterns and velocity magnitudes are qualitatively similar when there is a change in impeller speed and fluid viscosity, however comparison of the axial velocity component profiles still reveals a lack of self-similarity. Increasing the Reynolds number further to 3000, as shown in Fig. 5, results in mean velocity fields around the impeller that are independent of impeller speed and fluid viscosity, as would be expected for turbulent flow. However, although self-similarity is achieved at this Reynolds number in the vicinity of the impeller, fully-developed turbulent flow in the entire tank is not yet achieved. Indeed, the fluid velocity in the top third of the tank is very low so laminar flow would dominate in this zone. Using the relationship determined by Machado et al. (2013), the dimensionless height, y/H , at which turbulent flow should be achieved is 0.65. This is roughly the height at which the velocity magnitude is almost zero in Fig. 5.

3.1.2. POD eigenvalue spectra

Fig. 6 shows the eigenvalue spectrum for the case with different Reynolds number equal to 340, 980, and 3000. This corresponds to the energy contribution of each mode to the total kinetic energy of the system. According to the energy cascade theory, the lower modes (denoted as eigenvalue numbers in Fig. 6) are typically associated with large scale flow structures, such as trailing vortices and macro-instabilities, whilst the higher modes are related to smaller scale flow structures and turbulence. When two consecutive modes have similar contributions to the total energy, they may reveal large scale coherent structures, i.e. large scale flow patterns that are organised and persistent as opposed to occurring randomly (Moreau and Liné, 2006; Gabelle et al., 2013).

It can be seen in Fig. 6 that the energy contribution of the first mode generally decreases from about 18% to about 5% as the Reynolds number increases from $Re=340$ to 3000. This is expected since as the Reynolds number increases, energy is dissipated down to smaller scales in the flow. It is also observed that at $Re=340$, the impeller speed and fluid viscosity modify the eigenvalue spectrum. The modes associated with the large-scale flow structures have a greater contribution to the total energy in the flow when the impeller speed and fluid viscosity are low, whilst there is a higher energy contribution of the small-scale structures when the impeller speed and viscosity are high. This result suggests that the impeller speed,

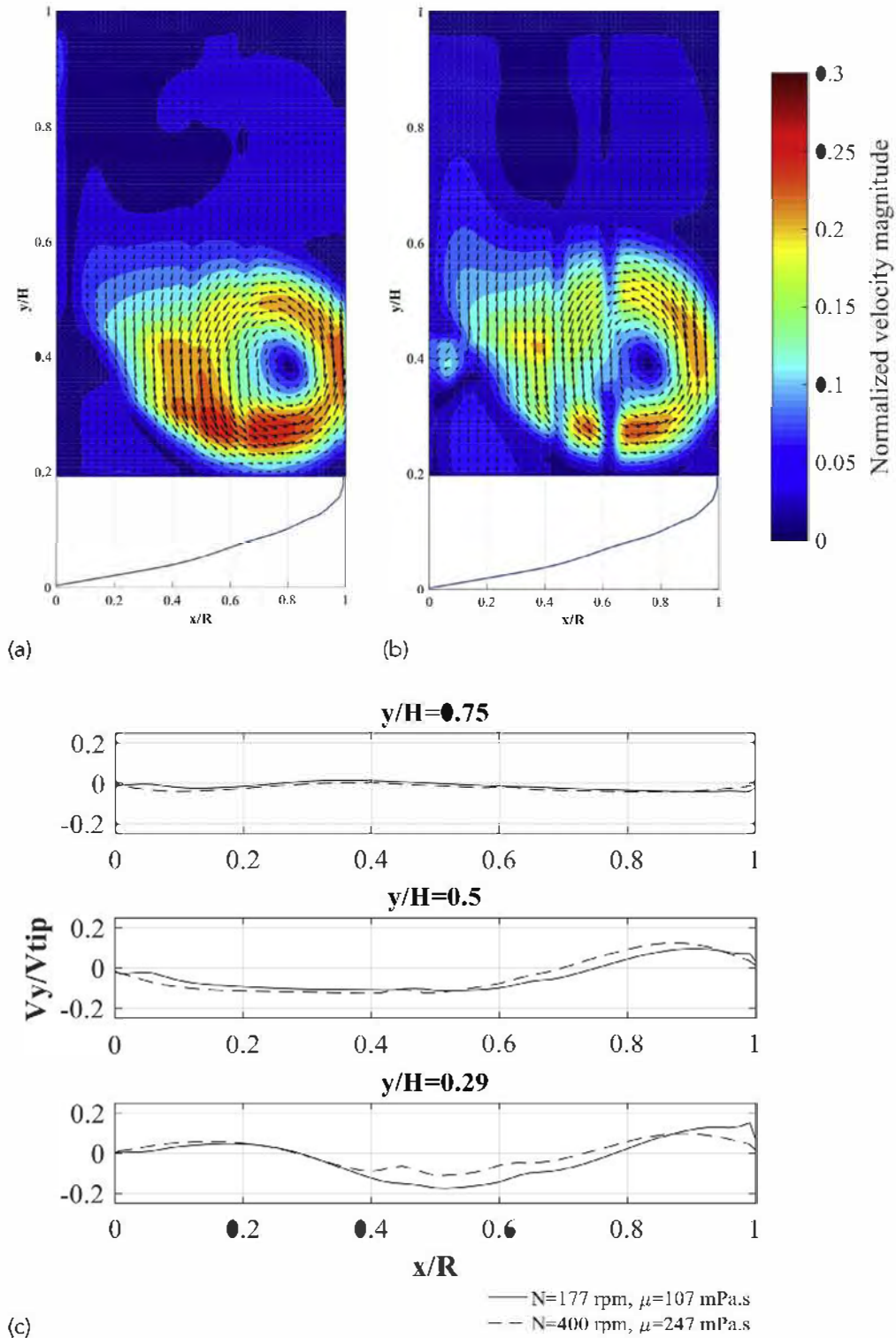


Fig. 3 – Mean velocity fields at $Re=340$. (a) $N=177$ rpm and $\mu=107$ mPa.s; (b) $N=400$ rpm and $\mu=247$ mPa.s; (c) comparison of normalized axial velocity profiles for both operating conditions.

and therefore inertia, is controlling the development of large-scale flow structures rather than the viscous effects, as would be expected. As Re increases, however the effect of the operating conditions on the eigenvalue spectra diminishes, which means that the flow structures are becoming similar in terms of energy distribution.

3.1.3. POD spatial eigenfunctions

As mentioned in Liang & Dong (2015), POD is a possible method for decoupling spatial coherent structures from temporal variations. The spatial structures, or eigenfunctions, are

presented in this section and their time-dependent behaviour determined from the time coefficients, $a_k^{(j)}(t)$, in the next section. It should be noted that the spatial structures do not correspond to velocity fields of actual vortices, but they give a qualitative sense of the type of structure that occur in the flow dynamics.

Figs. 7–9 show four spatial eigenfunctions for each of the cases at $Re=340, 980$ and 3000 . At $Re=340$, it is observed that when $N=177$ rpm the flow structures represented by modes 1 and 3 occupy the entire mid plane of the tank, whilst for modes 2 and 4 they are limited to the vicinity of the impeller. In

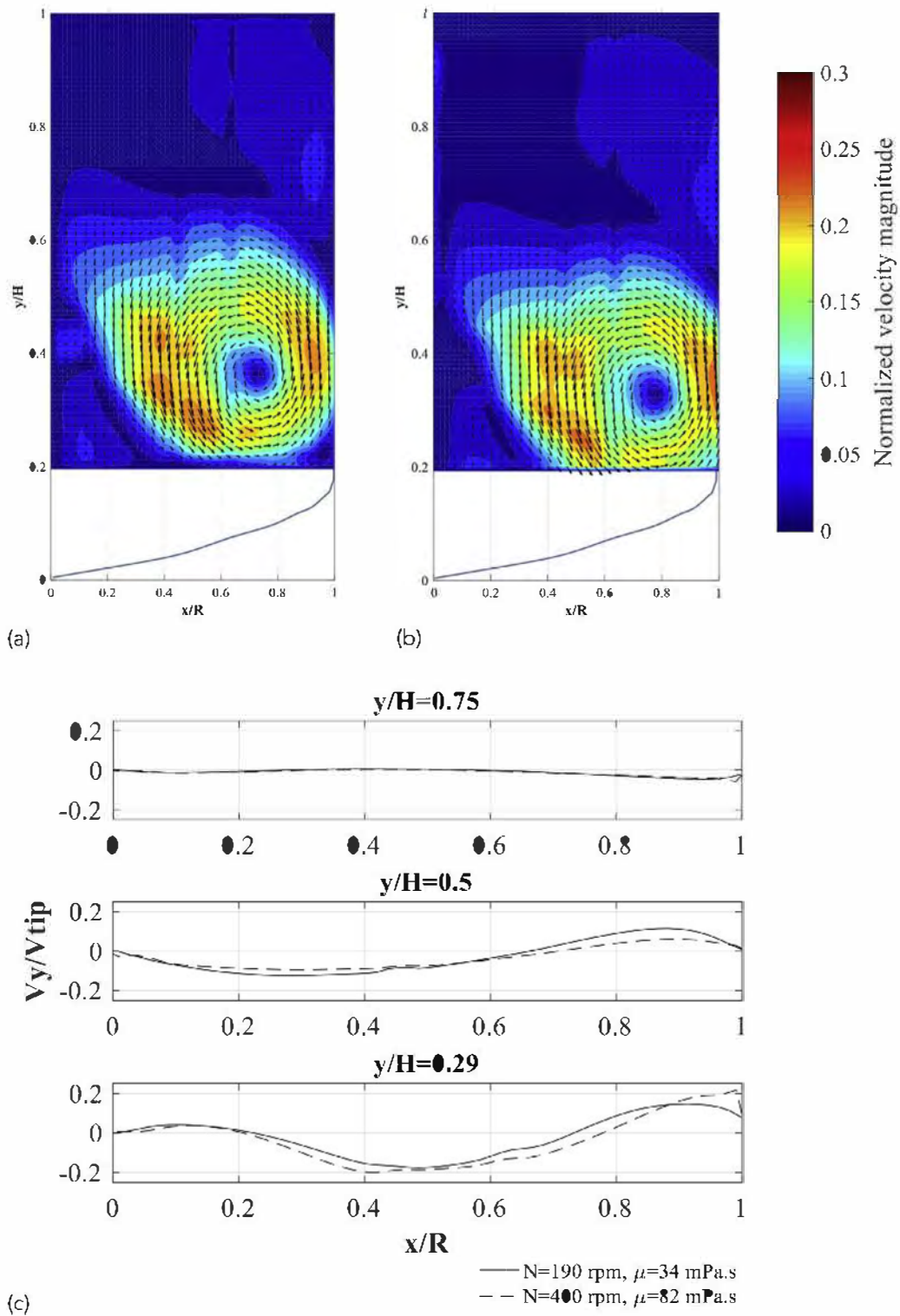


Fig. 4 – Mean velocity fields at $Re=980$. (a) $N=190$ rpm and $\mu=34$ mPa.s; (b) $N=400$ rpm and $\mu=82$ mPa.s; (c) comparison of normalized axial velocity profiles for both operating conditions.

contrast, when $N=400$ rpm, the structures depicted by modes 1 and 2 are restricted to a zone close to the impeller and modes 3 and 5 occupy the entire mid plane of the tank. It can also be seen that mode 1 at $N=177$ rpm (Fig. 7(a)) is structurally similar to mode 3 at $N=400$ rpm (Fig. 7(g)), and likewise for mode 3 at $N=177$ rpm and mode 5 at $N=400$ rpm. Note that no significant structures were present in modes 5 and 6 at $N=177$ rpm or modes 4 and 6 at $N=400$ rpm. It is noted that for both operating conditions at $Re=340$ the modes appear to be ‘shuffled’; one would expect similar flow structures to be in consecutive pairs and the larger structures to have the highest

eigenvalues (as seen later in the CFD data). The origin of this ‘shuffling’ of the modes is not clear at this stage.

At $Re=980$ and 3000 (Figs. 8 and 9), it can be seen that all of the flow structures in the first four to five modes fill most of the plane and that there are no structures that are only located in the vicinity of the impeller. It is also observed that at $Re=980$, the structures in modes 1 and 2 are hardly affected by the operating conditions. This suggests that there is almost no difference in the macro flow dynamics because its two most energetic flow structures are very similar. Sim-

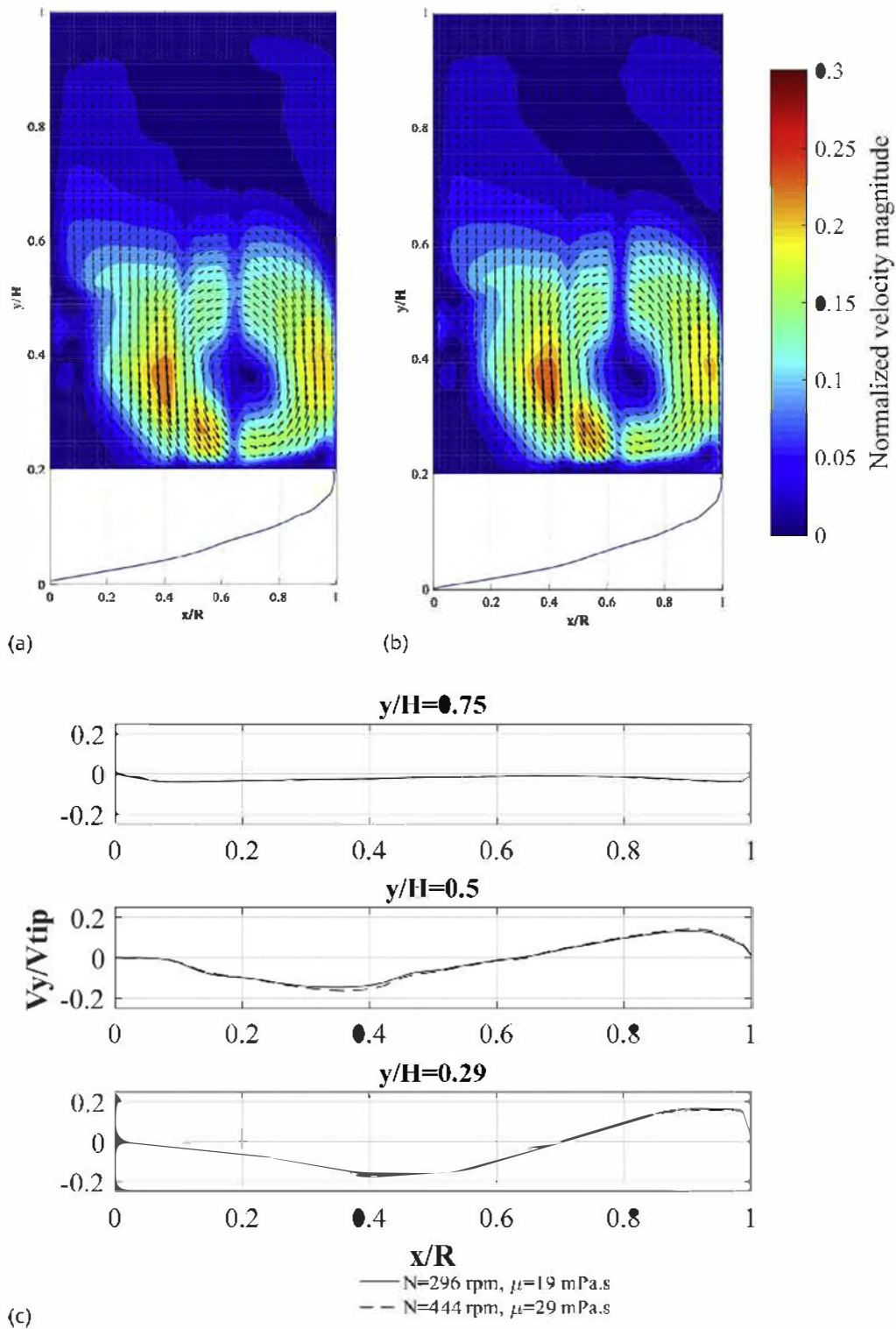


Fig. 5 – Mean velocity fields at $Re=3000$. (a) $N=296$ rpm and $\mu=19$ mPa.s; (b) $N=431$ rpm and $\mu=28$ mPa.s; (c) comparison of normalized axial velocity profiles for both operating conditions.

ilarly, at $Re=3000$, the flow structures for modes 1–3 appear to be independent of the operating conditions. It is therefore possible to deduce that as the Reynolds number increases, the dynamics of the flow becomes more robust and less sensitive to changes in impeller speed and fluid properties.

3.1.4. POD time coefficients

The POD methodology not only provides information on the spatial structures in a flow, it also allows a temporal analysis of the flow structures. The time coefficients obtained by POD may be considered as weights, which are assigned to the instanta-

neous velocity fields, providing information on the fraction of mode I that is contained in the instantaneous velocity field i . Analyses of the time coefficients – e.g. via phase portraits and Fast Fourier Transforms – enable one to determine if two spatial modes are related and if they contribute to coherent structures, or if there are dominant frequencies occurring in the flow.

3.1.4.1. Phase portrait. Fig. 10 shows phase portraits, where the time coefficients for two spatial modes are plotted against one another, for $Re=340$ for the two different operating con-

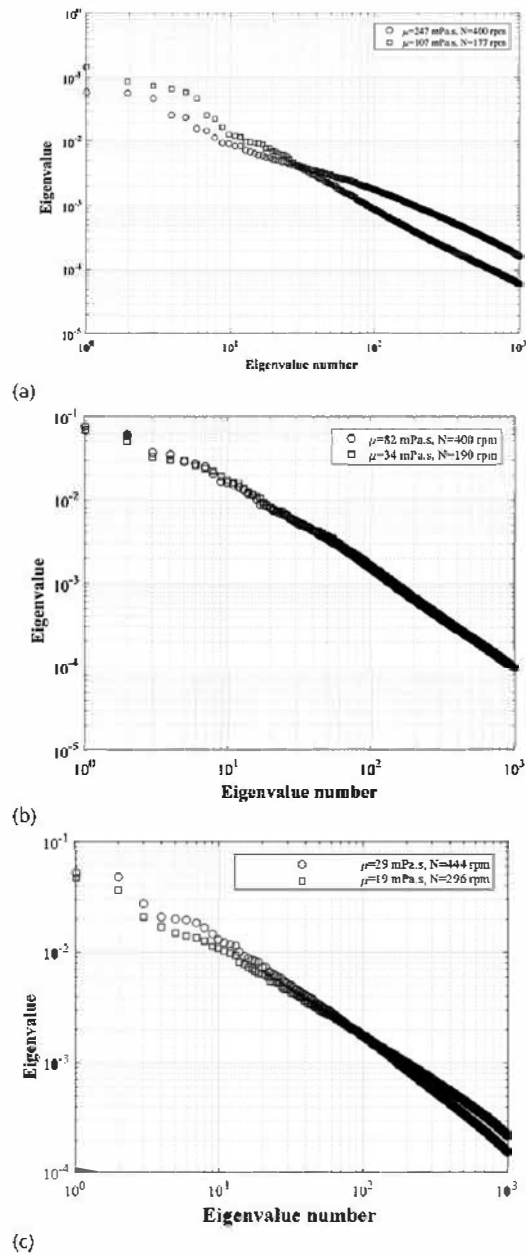


Fig. 6 – Eigenvalue spectra extracted from the experimental data. (a) $Re = 340$, (b) $Re = 980$, (c) $Re = 3000$.

ditions. The circular or elliptical shape of the phase portrait implies that there is a periodic relationship between the two modes and that they make a coherent structure. Note that two consecutive modes are not necessarily plotted together here since the ordering of modes is somewhat shuffled due as discussed in the previous section. In the low impeller speed and viscosity case, Fig. 10(a) and (b), modes 1 and 3 are coupled and modes 2 and 4 are coupled. Indeed, as seen in Fig. 7, the spatial structures of modes 1 and 3 are similar in the fact that they fill the 2-dimensional measurement plane, and likewise for modes 2 and 4, where the spatial structures are limited to the zone around the impeller. Similar observations can be made for the case where $N = 400$ rpm and $\mu = 247$ mPa.s.

At $Re = 980$ and 3000 , however, the phase portraits did not reveal the existence of any periodic coherent structures, at least not in the large plane of measurement considered in this work. Nevertheless, it is possible that in a smaller zone of measurement, e.g. an area restricted to the vicinity of the impeller, coherent structures may be found.

3.1.4.2. Analysis of frequencies. The time coefficients establish a spatial-temporal relationship between the eigenfunctions and the instantaneous velocity fields that represent the temporal evolution of the different modes. As a consequence, it is possible to obtain the power spectrum of a mode by performing a Fast Fourier transformation of the corresponding sequence of time coefficients. Fig. 11 shows the power spectra associated with the spatial modes given in Fig. 7 that have been determined by FFT of the associated time coefficients. For the low impeller speed and viscosity case (Fig. 11(a)–(d)), it is not surprising to see that mode pairs associated with coherent structures, i.e. modes 1 and 3, and modes 2 and 4, have the same dominant frequency, $0.14N$ and $0.08N$, respectively. A similar observation is made for the higher impeller speed and viscosity case, where modes 1 and 2, and modes 3 and 5 have the same dominant frequencies of $0.31N$ and $0.16N$, respectively. It is interesting to point out that although the space filling structures have similar frequencies regardless of the operating conditions (compare Fig. 11(a) and (c) where $f = 0.14N$ and Fig. 11(g) and (h) where $f = 0.16N$), the fre-

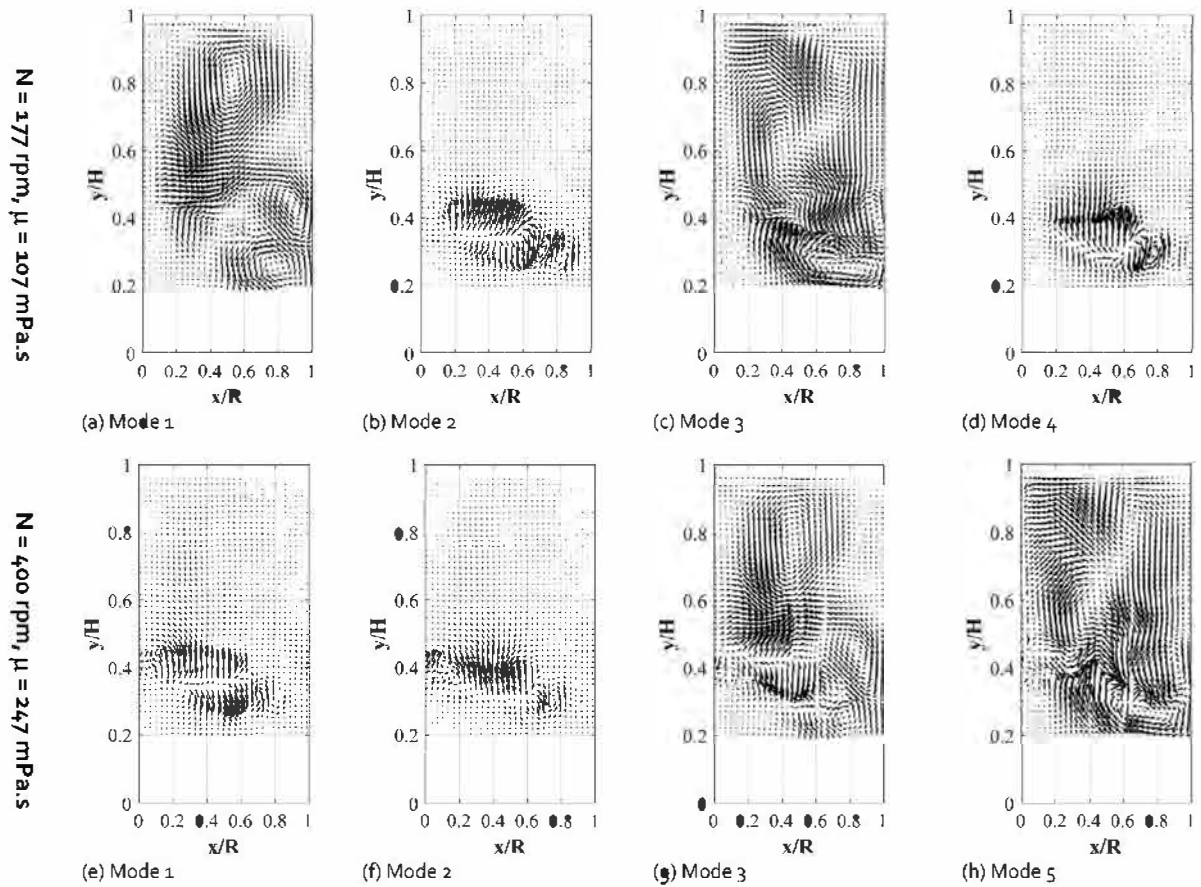


Fig. 7 – Spatial eigenfunctions for $Re = 340$. (a)–(d) correspond to $N = 177$ rpm and $\mu = 107$ mPa s. (e)–(h) correspond to $N = 400$ rpm and $\mu = 247$ mPa s.

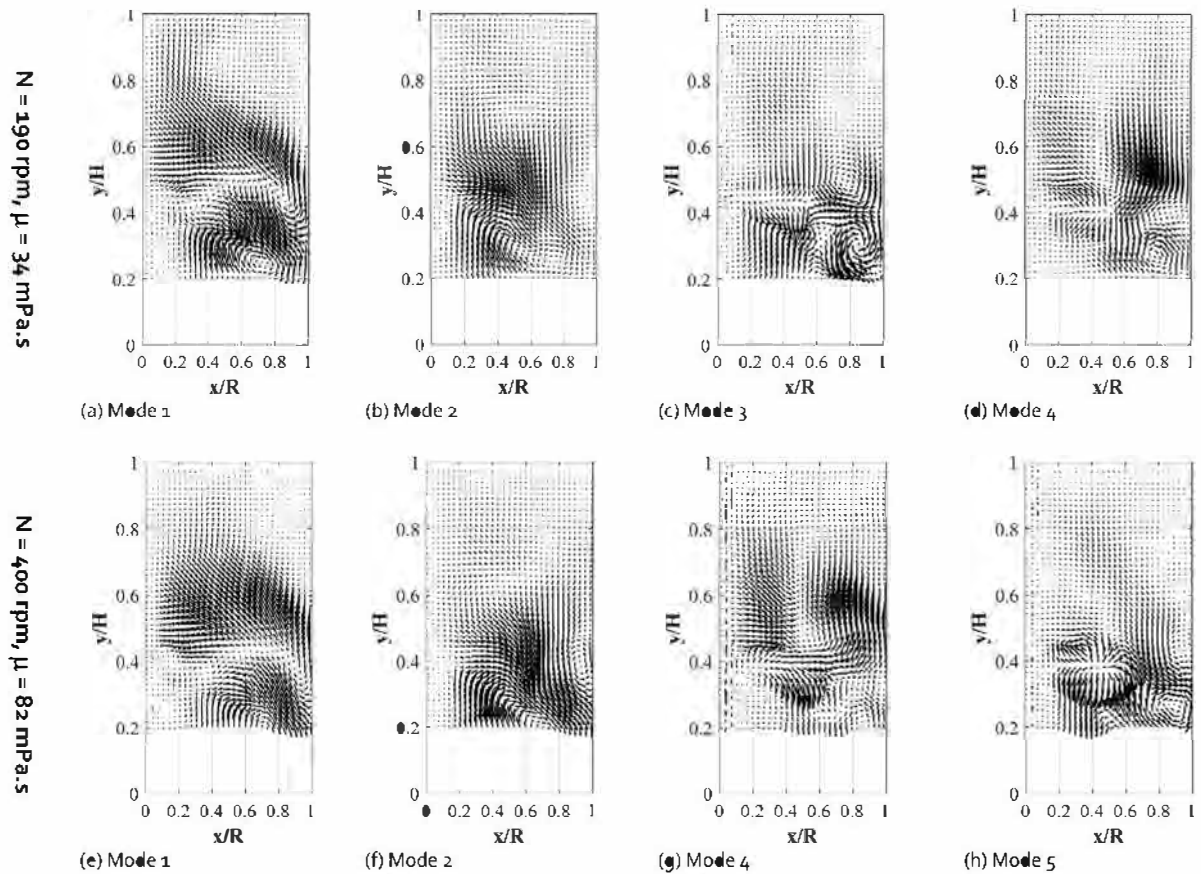


Fig. 8 – Spatial eigenfunctions for $Re = 980$. (a)–(d) correspond to $N = 190$ rpm and $\mu = 34$ mPa s. (e)–(h) correspond to $N = 400$ rpm and $\mu = 82$ mPa s.

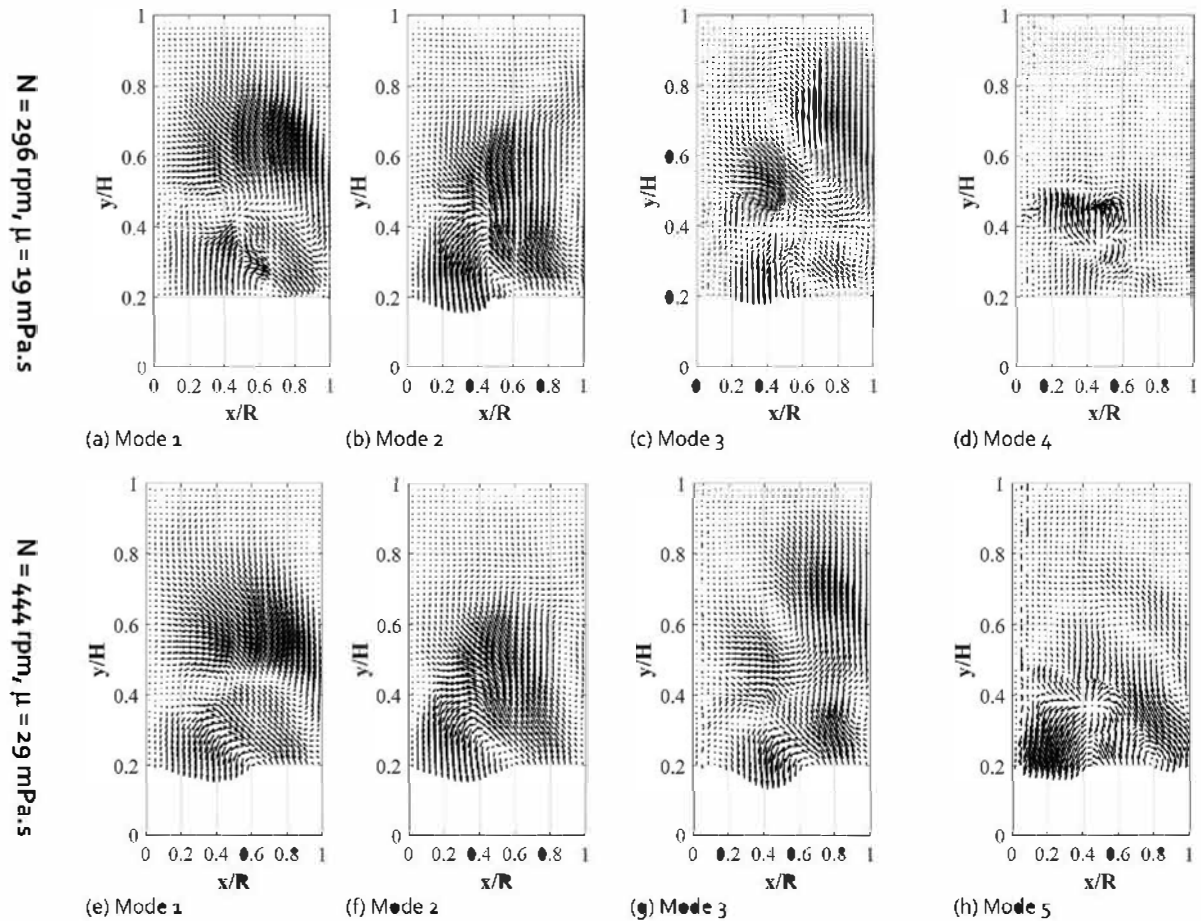


Fig. 9 – Spatial eigenfunctions for $Re=3000$. (a)–(d) correspond to $N=296$ rpm and $\mu=19$ mPa s. (e)–(h) correspond to $N=444$ rpm and $\mu=29$ mPa s.

quencies of the structures that are restricted to the impeller zone are clearly dependent on the operating conditions. The frequency of these structures obtained with $N=400$ rpm and $\mu=247$ mPa s is almost four times that for the case where $N=177$ rpm and $\mu=107$ mPa s. A further difference in the two operating conditions is the existence of a secondary frequency in mode 1 and mode 3 for the high impeller speed and viscosity case that is equal to the dominant frequency of mode 3 and mode 1, respectively. The origin of these different frequencies, which depend on the operating conditions, is not entirely clear from the results presented here. In order better understand the trends of the observed frequencies and to correlate them with the underlying flow structures, a larger campaign of measurements at low Reynolds number and with varying impeller speed and fluid viscosity would be required.

At $Re \geq 980$, the characteristic frequencies become less dominant since coherent structures in the flow are absent. Nevertheless, prevailing frequencies can still be identified. Table 2 shows the frequencies identified for the first and second modes at the different operating conditions and $Re=340$, 980 and 3000. It can be seen that the frequency identified for the first mode at $Re=980$ and 3000 is $0.03N$, which is an order of magnitude lower than the values obtained at $Re=340$. The frequency of the second mode, however, is around $0.12N$, except for the low impeller speed and viscosity case at $Re=3000$ where the value is $0.02N$. It is interesting to point out that the frequencies identified for the cases where $Re \geq 980$ are very similar to those identified for the precessing vortex macro-instability at transitional flow Reynolds numbers by Galletti et al. (2004) and Ducci et al. (2008). They identified two fre-

quencies: one at $0.02N$, which was attributed to the off-centred precession of the vortex core, and the other $0.12N$, which was related to the elongation of the vortex core and its rotation around its own axis. They found that as Re increases, the low frequency $0.02N$ peak is associated with the most energetic modes. Indeed, the results of this study for $Re \geq 980$ show low frequency for mode 1 and high frequency for mode 2, except for the case at $Re=3000$ with low impeller speed and viscosity where the low frequency prevails in mode 2. The similarity of these results with those of Galletti et al. (2004) and Ducci et al. (2008) strongly suggests that the instabilities detected here are related to the vortex, which may be described as a large coherent structure that is convected by the mean flow (Kresta and Roussinova, 2004). There is clearly a significant difference in the behaviour of the flow structures at $Re \geq 980$ and at $Re < 980$. At $Re < 980$, the frequencies depend strongly on the operating conditions and fluid properties, whilst at $Re \geq 980$ the frequencies are quasi-independent of fluid properties, which is in agreement with Galletti et al. (2004). Note that although there appears to be an effect of the impeller speed and viscosity on the frequency of mode 2 at $Re=3000$, it is pointed out that the frequency of mode 3 is $0.12N$ for the low viscosity case and $0.03N$ for the high viscosity case. Considering experimental error and consequent shuffling of modes, it can be considered that there is little effect of operating conditions on the flow at $Re=3000$. Furthermore, the appearance of the low frequency ($0.02N$) in the lower modes suggests that as the Reynolds number increases, the off-centred precession of the vortex core dominates, as observed in previous studies (Galletti et al., 2004; Ducci et al., 2008).

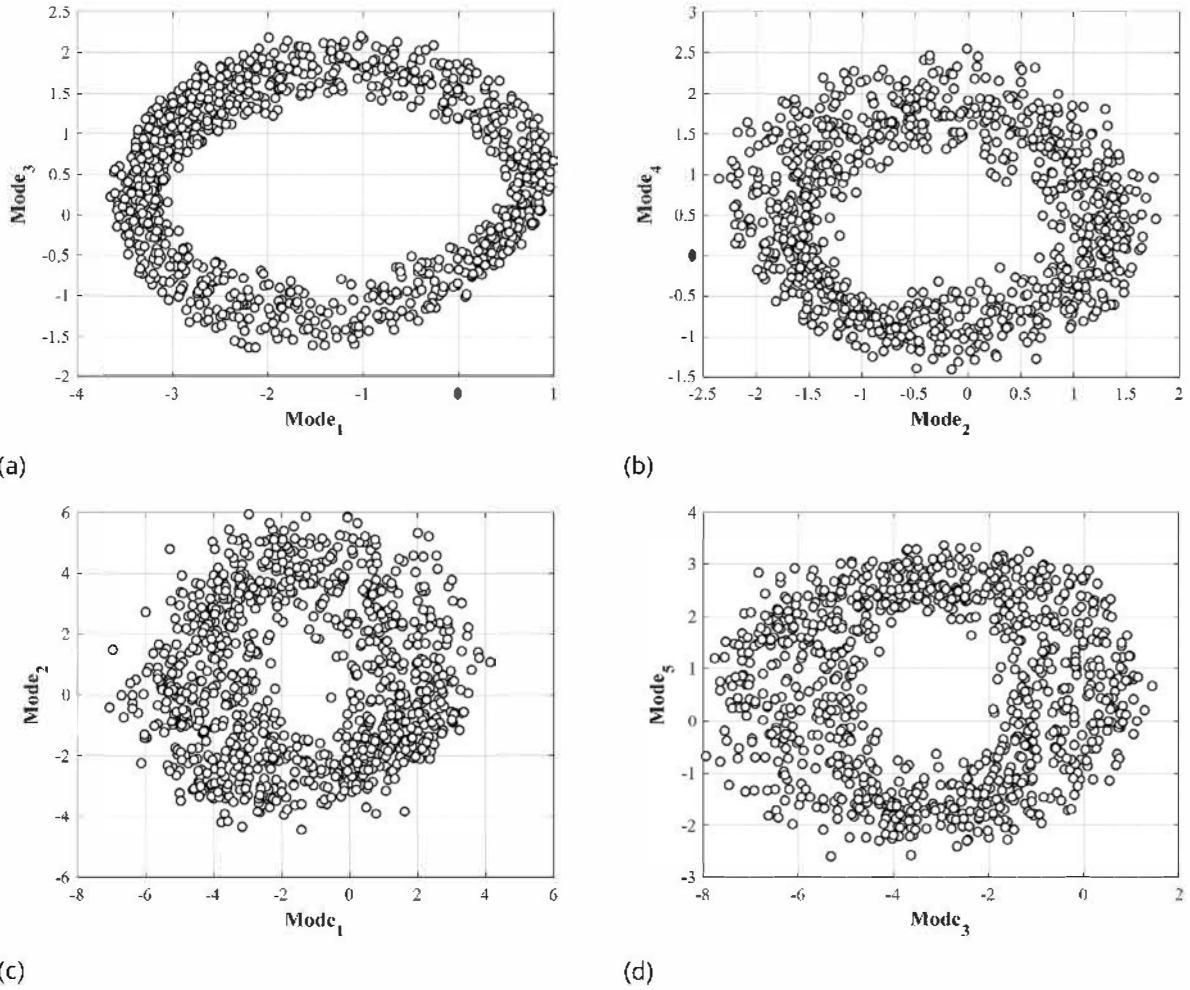


Fig. 10 – Phase portrait of coefficients for $Re = 340$. (a), (b) correspond to $N = 177$ rpm and $\mu = 107$ mPa s. (c), (d) correspond to $N = 400$ rpm and $\mu = 247$ mPa s.

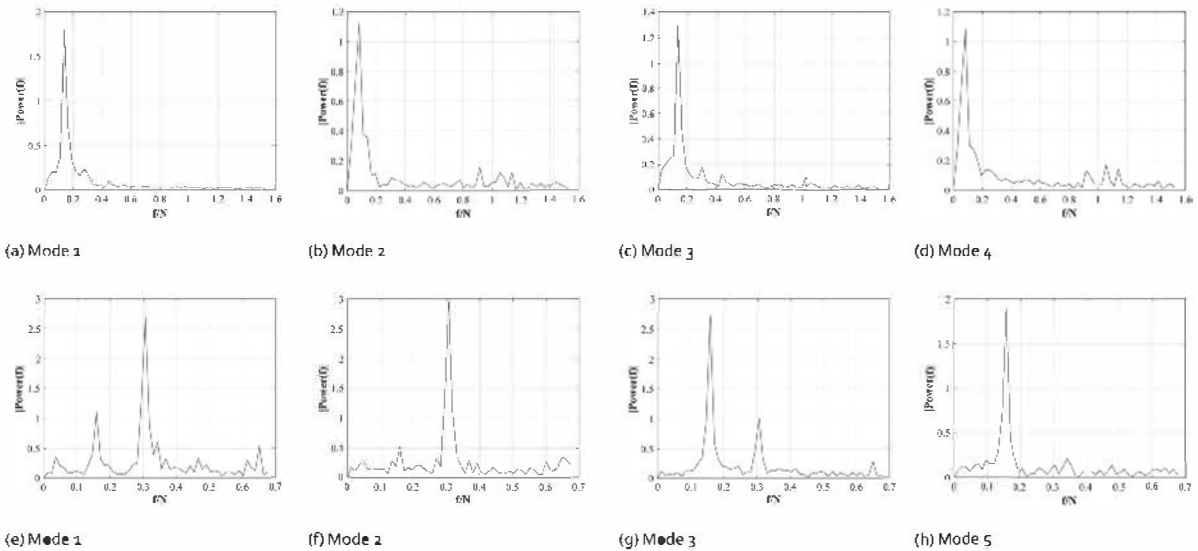


Fig. 11 – FFT analysis of time coefficients at $Re = 340$. (a)–(d) correspond to $N = 177$ rpm and $\mu = 107$ mPa s. (e)–(h) correspond to $N = 400$ rpm and $\mu = 247$ mPa s.

3.2. Simulation of flow at $Re = 340$

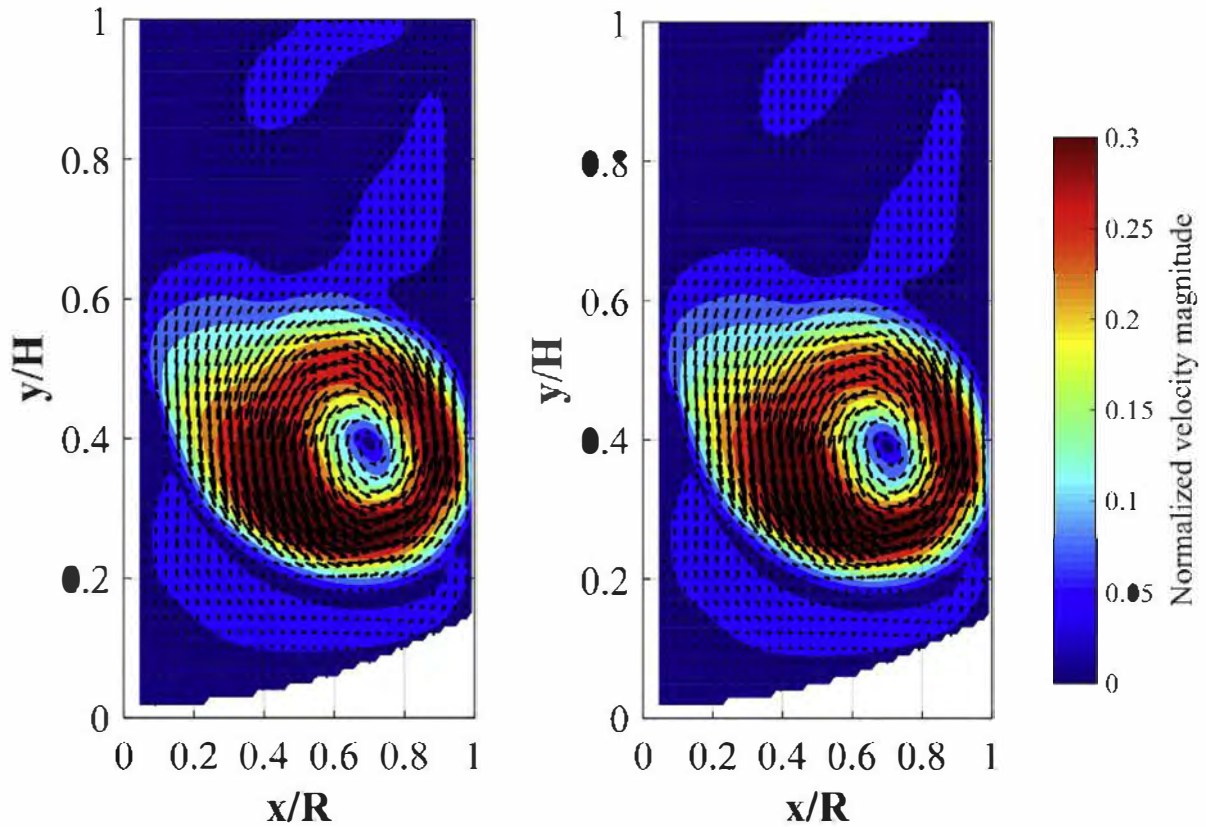
In this section, numerical results for the two cases with different impeller speed and viscosity at $Re = 340$, where experimental data show a lack of self-similarity, are presented.

3.2.1. Mean flow

Fig. 12 presents contour plots of the mean velocity field for the two different operating conditions at $Re = 340$ and the axial velocity profiles compared with experimental results. It can be seen that there is no effect of impeller speed and fluid viscosity on the mean flow fields, which contrasts with the experimen-

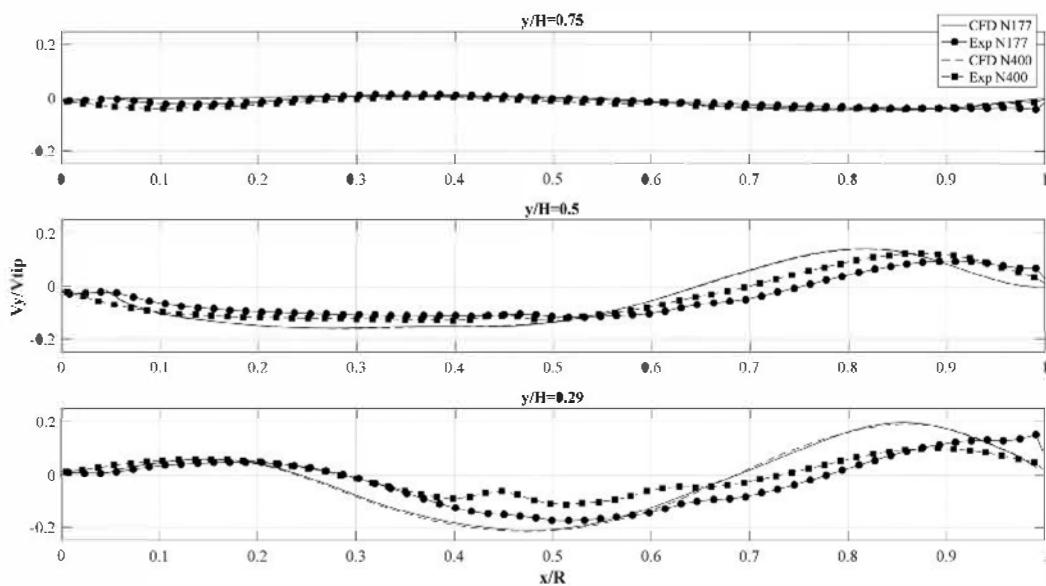
Table 2 – Frequencies identified for modes 1 and 2 of the cases studied at different Reynolds numbers.

| Re | N (rpm) | μ (mPa s) | Frequency mode 1, f_1 | Frequency mode 2, f_2 |
|------|---------|---------------|-------------------------|-------------------------|
| 340 | 177 | 107 | 0.14N | 0.08N |
| 340 | 400 | 247 | 0.31N | 0.31N |
| 980 | 190 | 34 | 0.03N | 0.13N |
| 980 | 400 | 82 | 0.03N | 0.13N |
| 3000 | 296 | 19 | 0.03N | 0.02N |
| 3000 | 444 | 29 | 0.03N | 0.12N |



(a)

(b)



(c)

Fig. 12 – Simulated mean velocity fields at $Re = 340$. (a) $N = 177$ rpm and $\mu = 107$ mPa s; (b) $N = 400$ rpm and $\mu = 247$ mPa s; (c) comparison of normalized axial velocity profiles for both operating conditions.

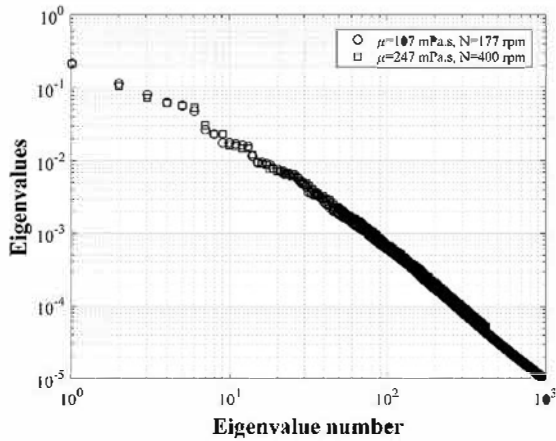


Fig. 13 – Eigenvalue spectrum for numerical data obtained with different operating conditions at $Re = 340$.

tal measurements given in Fig. 3. Although the experimental and numerical flow fields are qualitatively similar in terms of flow pattern and velocity magnitude, the CFD simulations predict higher velocities in the circulation loop and self-similarity; this can be clearly seen with the axial velocity profiles in Fig. 12(c).

3.2.2. POD analysis

The energy spectrum for the numerical data obtained at $Re = 340$ and sampled at 9 Hz is shown in Fig. 13. It can be seen that the eigenvalues of each mode (or eigenvalue number) are quasi-identical, which means that the energy level of each of the eigenfunctions and their relevance in terms of

flow dynamics are not affected by impeller speed or viscosity, as observed in the experiments.

Fig. 14 compares the spatial eigenfunctions obtained with the simulated data for the two sets of operating conditions at $Re = 340$. Similarly to what was observed in Figs. 12 and 13, there is no effect of impeller speed or fluid viscosity on the eigenfunctions obtained with the numerical flow fields. Both modes 1 and 2 show a flow structure that fills the whole measurement plane, whilst the structures for the following modes are restricted to the vicinity of the impeller swept volume. Although the simulations predict self-similarity and the experimental measurements do not, the general flow structures predicted by the simulations are in very good agreement with those found experimentally, as shown in Figs. 7 and 14 (even though the mode numbers do not always correspond). This means that the CFD model is capable of correctly replicating the most energetic structures of flow dynamics. Similarly, the analysis of the time coefficients via the plotting of phase portraits reveals that two coherent structures exist for both sets of operating conditions, like those observed for the experimental data. Table 3 shows the frequencies of the time coefficients and it can be seen that they too are largely independent of impeller speed and fluid viscosity. These frequencies are not exactly the same as found experimentally, but fall approximately mid-way between each of the experimental values.

In the comparison of the PIV and CFD results, care was taken to make the sampling frequency of the numerical data the same as that used experimentally, i.e. 9 Hz. However, in the simulations, data were stored at a higher frequency in order to examine the effect on the POD analysis. Fig. 14(a) and (b) com-

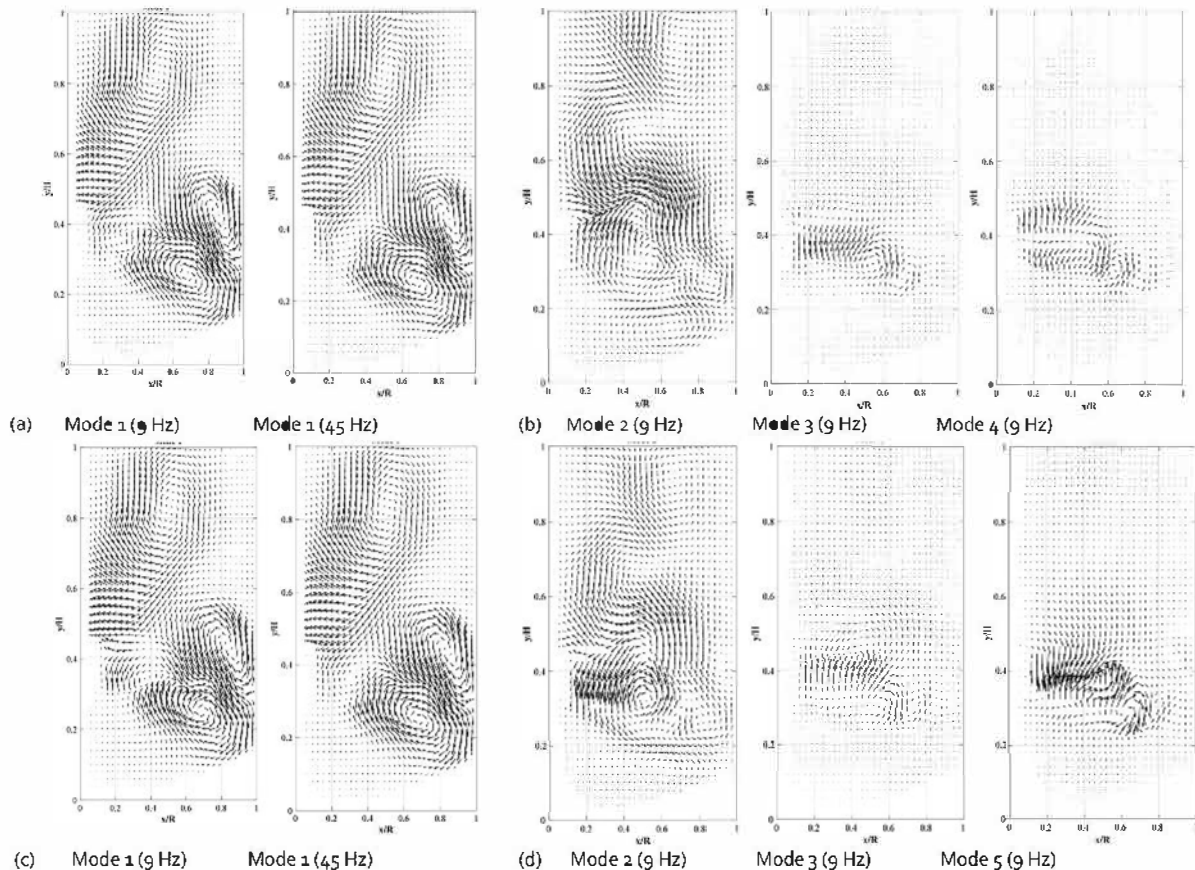


Fig. 14 – Spatial eigenfunctions for different modes obtained from numerical data for $Re = 340$ where (a), (b) $N = 177$ rpm and $\mu = 107$ mPa s and (c), (d) $N = 400$ rpm and $\mu = 247$ mPa s. The effect of sampling frequencies of 9 Hz and 45 Hz on Mode 1 is given in (a) and (c).

Table 3 – Frequencies identified for the different eigenfunctions obtained with the numerical data sampled at 9 Hz and 45 Hz.

| Sampling frequency (Hz) | N (rpm) | μ (mPa s) | Frequency mode 1, f_1 | Frequency mode 2, f_2 |
|-------------------------|---------|---------------|-------------------------|-------------------------|
| 9 | 177 | 107 | 0.23N | 0.23N |
| 9 | 400 | 247 | 0.24N | 0.24N |
| 45 | 177 | 107 | 0.23N | 0.23N, 2.97N |
| 45 | 400 | 247 | 0.24N | 0.24N, 2.93N |

compares the spatial eigenfunctions of mode 1 obtained with a sampling frequency of 9 Hz and 45 Hz. Clearly, there is no effect of this parameter on the flow structures. It can also be seen in Table 3 that the associated time coefficients are the same regardless of the sampling frequency except for the fact that the impeller blade passing frequency (equal to $3N$) is picked up as a secondary frequency when the data are sampled at 45 Hz.

3.3. Discussion on flows at $Re = 340$

Whilst the previous sections show reasonable agreement between the experimental and CFD results of the flows obtained at $Re = 340$, the CFD results predict self-similarity of mean velocities, which was not observed experimentally, and the spatial and temporal features of the experimental and simulated flow structures are not exactly the same. Extreme caution was taken in the CFD simulations to ensure a very fine mesh (6.4 million cells), grid independence, a small time-step (0.8 ms for the high N case), a RMS Courant number of 0.5 and a long simulation time (300 impeller revolutions, at a computation cost of 1.4 h of CPU on 24 cores per impeller revolution) and it can therefore be considered that the simulations are more or less error-free. Furthermore, scaling the terms in the Navier–Stokes equations would suggest that the CFD result of self-similarity is correct, as the results should depend on the Reynolds number with the time-scales ‘stretched’ by the impeller rotation rate. The reason(s) for the apparent discrepancies between the experimental and numerical results are therefore not straightforward. A simulation in which the air-liquid free surface was modelled, and therefore the Froude number was introduced, showed this did not explain the results.

One possible explanation for the observed differences is the fact that the simulations are physically perfect but the experiments are not. Indeed, there are always physical imperfections of any experimental set-up, and in the current case these may include slight differences in the vessel and impeller geometry, as well as non-uniform impeller speed and imperfect shaft alignment. The latter can lead the shaft and impeller to wobble and vibrate, which will introduce another degree of freedom (even if the physical perturbation is very small) that is not accounted for in the simulations. It is highly possible that this could lead to non-self-similar velocity profiles. This therefore suggests that an additional dimensionless group, e.g. some form of Strouhal number involving the spatial and temporal scales of the ‘imperfections’, may be required in the simulations in order to predict the behaviour observed experimentally.

The experimental results of this study have shown that the operating conditions – impeller rotation speed and fluid viscosity – clearly affect the flow dynamics in the stirred tank at low Reynolds number ($Re = 340$) but such effects decrease with increasing turbulence, i.e. as the Reynolds number increases to 980 and then to 3000. This suggests that the higher Reynolds number flows are more resilient to changes in operating condi-

tions and small physical perturbations, whilst lower Reynolds number flows are much more sensitive to such changes. Indeed, similar observations have been made in many other systems. For example, heat transfer rates are highly sensitive to thermal boundary conditions in laminar and transitional flows but are independent of boundary conditions if the flow is fully turbulent. Introducing pump ‘noise’ in a simulation of microchannel flow can create the onset of chaotic flow, which is observed experimentally but otherwise not predicted (Dai et al., 2015). Dynamic flow perturbations, such as time-dependent impeller rotation in laminar stirred tanks, can also generate chaotic flow (Lamberto et al. 2001).

4. Conclusions

Experimental and numerical data of flow in a stirred tank in the transitional flow regime has been analysed via mean flow fields and using Proper Orthogonal Decomposition. The effects of impeller rotation speed and fluid viscosity on the flow structures have been investigated.

Experimentally, it has been found that the mean dimensionless velocity fields are self-similar at $Re = 3000$ but this self-similarity decreases as the Reynolds number decreases to 980 and 340. At $Re = 340$, the flow fields are clearly dependent on impeller speed and fluid viscosity. Analysis using POD allows the flows to be compared in terms of dominant spatial structures and characteristic times. Coherent flow structures are identified at $Re = 340$ only and the time coefficients for these structures also vary with impeller speed and fluid viscosity. As the Reynolds number increases from 340 to 3000, however, the dynamics of the flow become more robust and less sensitive to changes in impeller speed and fluid viscosity. At the higher Reynolds numbers, two dominant frequencies at 0.03N and 0.13N are observed in the flow structures; these are very similar to the frequencies previously identified for precessing vortex macro-instabilities in transitional flows (Galletti et al., 2004; Ducci et al., 2008).

Transient laminar simulations of flow at $Re = 340$ and with different impeller speeds and fluid viscosities have been performed using a very fine computational mesh. The mean velocity fields are in reasonable agreement with the experimental measurements, however they predict self-similarity of velocity profiles and there is no apparent effect of impeller speed or viscosity, which is unlike the experimental observations. Analysis of the flow using POD also reveals that the predicted flow structures are identical regardless of the operating conditions, which also contradicts the experimental results. It is believed that physical perturbations due to imperfections in the experimental setup may be the cause of such differences in the flow when the Reynolds number is low. Indeed, it appears that at low Reynolds numbers, the flow is highly sensitive to small changes in operating conditions, whilst it becomes more resilient to perturbations at higher Reynolds numbers.

These results demonstrate the difficulty of validating CFD simulations of flows in the transitional regime because they are sensitive to small changes in operating conditions. Indeed, small imperfections in an experiment may cause significant changes in the flows generated but these imperfections are most often ignored in the simulation. If both the experiments and the CFD simulations are carefully performed, neither of the results are wrong; it is just a case of comparing two datasets that do not have perfectly identical conditions.

Notation

| | |
|-------------|---|
| $a_k^{(l)}$ | Time coefficient of mode l for event k |
| C | Off-bottom clearance [m] |
| C | Auto-correlation matrix [$m^2 s^{-2}$] defined in Eq. (3) |
| d_p | Diameter of PIV seeding particle [m] |
| D | Diameter of impeller [m] |
| f | Frequency [Hz] |
| H | Height of tank [m] |
| i | Instantaneous velocity field number |
| I | Mode number |
| M | Snapshot matrix [$m s^{-1}$] defined in Eq. (4) |
| n | Number of snapshots |
| N | Impeller rotation rate [rpm] |
| Re | Reynolds number |
| s | Shaft diameter [m] |
| T | Diameter of tank [m] |
| t | Time [s] |
| u | Cartesian velocity component in the x -direction [$m s^{-1}$] |
| V_{tip} | Impeller tip speed, πND [$m s^{-1}$] |
| \vec{V} | Velocity vector [m] |
| w | Baffle width [m] or Cartesian velocity component in the z -direction [$m s^{-1}$] |
| x, y, z | Cartesian coordinates [m] |

Greek symbols

| | |
|-----------------------|--|
| λ | Eigenvalue |
| μ | Dynamic viscosity [Pa s] |
| ρ | Fluid density [$kg m^{-3}$] |
| $\vec{\varphi}^{(l)}$ | Eigenvector of mode l [$m s^{-1}$] |

Subscripts

| | |
|------|----------------------------------|
| k | Event number in sequence of data |
| mean | Time mean |

Superscripts

| | |
|-----|-------------|
| I | Mode number |
| T | Transpose |

Acknowledgements

The authors gratefully acknowledge Prof. A. Liné (INSA, Université de Toulouse) for sharing his valuable expertise on POD. The authors are also thankful to R. Kehn (SPX Flow) for having provided the A320 impeller geometry for the CFD simulations. The authors acknowledge the facilities and the technical assistance of the Sydney Informatics Hub at the University of Sydney and, in particular, access to the high-performance computing facility Artemis.

References

Alberini, F., Liu, L., Stitt, E.H., Simmons, M.J.H., 2017. [Comparison between 3-D-PTV and 2-D-PIV for determination of](#)

- [hydrodynamics of complex fluids in a stirred vessel](#). *Chem Eng Sci* 171, 189–203.
- Berkooz, G., Holmes, P., Lumley, J., 1993. [The proper orthogonal decomposition in the analysis of turbulent flows](#). *Annu Rev Fluid Mech* 25 (1), 539–575.
- Bruha, O., Fort, I., Smolka, P., Jahoda, M., 1996. [Experimental study of turbulent macro-instabilities in an agitated system with axial high-speed impeller and radial baffles](#). *Collect Czechoslov Chem Commun* 61, 856–867.
- Dai, Z., Zheng, Z., Fletcher, D.F., Haynes, B.S., 2015. [Experimental study of transient behaviour of laminar flow in zigzag semi-circular microchannels](#). *Exp Therm Fluid Sci* 68, 644–651.
- Derksen, J.J., 2011. [Direct flow simulations of thixotropic liquids in agitated tanks](#). *Can J Chem Eng* 89, 628–635.
- Derksen, J.J., 2012a. [Direct simulations of mixing of liquids with density and viscosity differences](#). *Ind Eng Chem Res* 51, 6948–6957.
- Derksen, J.J., 2012b. [Highly resolved simulations of solids suspension in a small mixing tank](#). *AIChE J* 58 (10), 3266–3278.
- Derksen, J.J., 2013. [Simulations of mobilization of Bingham layers in a turbulently agitated tank](#). *J Non Newt Fluid Mech* 191, 25–34.
- Ducci, A., Dougerakis, Z., Yianneskis, M., 2008. [Decomposition of flow structures in stirred reactors and implications for mixing enhancement](#). *Ind Eng Chem Res* 47 (10), 3664–3676.
- Ducci, A., Yianneskis, M., 2007. [Vortex tracking and mixing enhancement in stirred processes](#). *AIChE J* 53 (2), 305–315.
- Gabelle, J.-C., Morchain, J., Anne-Archard, D., Augier, F., Liné, A., 2013. [Experimental determination of the shear rate in a stirred tank with a non-Newtonian fluid: Carbopol](#). *AIChE J* 59 (6), 2251–2266.
- Galletti, C., Paglianti, A., Lee, K.C., Yianneskis, M., 2004. [Reynolds number and impeller diameter effects on instabilities](#). *AIChE J* 50 (9), 2050–2063.
- Hemrajani, R.R., Tatterson, G.B., 2004. [Mechanically stirred vessels](#). In: Paul, E.L., Atiemo-Obeng, V.A., Kresta, S.M. (Eds.), *Handbook of Industrial Mixing: Science and Practice*. John Wiley & Sons, Hoboken, NJ (Chapter 6).
- Holmes, P.J., et al., 1997. [Low-dimensional models of coherent structures in turbulence](#). *Phys Rep* 287, 337–384.
- Kresta, S.M., Roussinova, V.T., 2004. [Comments to On the origin, frequency and magnitude of macro-instabilities of the flows in stirred vessels by Nikiforaki et al.](#) *Chem Eng Sci* 59, 951–953.
- Lamberto, D.J., Alvarez, M.M., Muzzio, F.J., 2001. [Computational analysis of regular and chaotic mixing in a stirred tank reactor](#). *Chem Eng Sci* 56, 4887–4899.
- Liang, Z., Dong, H., 2015. [On the symmetry of proper orthogonal decomposition modes of a low-aspect-ratio plate](#). *Phys Fluids* 27 (6), 063601.
- Liné, A., Gabelle, J.-C., Morchain, J., Anne-Archard, D., Augier, F., 2013. [On POD analysis of PIV measurements applied to mixing in a stirred vessel with a shear thinning fluid](#). *Chem Eng Res Des* 91 (11), 2073–2083.
- Machado, M.B., Bittorf, K.J., Roussinova, V.T., Kresta, S.M., 2013. [Transition from turbulent to transitional flow in the top half of a stirred tank](#). *Chem Eng Sci* 98, 218–230.
- Machado, M.B., Kresta, S.M., 2013. [The confined impeller stirred tank \(CIST\): a bench scale testing device for specification of local mixing conditions required in large scale vessels](#). *Chem Eng Res Des* 91, 2209–2224.
- Montes, J.-L., Boisson, H.-C., Fort, I., Jahoda, M., 1997. [Velocity field macro-instabilities in an axially agitated mixing vessel](#). *Chem Eng J* 67, 139–145.
- Moreau, J., Liné, A., 2006. [Proper orthogonal decomposition for the study of hydrodynamics in a mixing tank](#). *AIChE J* 52, 2651–2655.
- Sirovich, L., 1987. [Turbulence and the dynamics of coherent structures part I: coherent structures](#). *Quart Appl Math* XLV 3, 561–571.
- Zhang, Y., Gao, Z., Li, Z., Derksen, J.J., 2017. [Transitional flow in a Rushton turbine stirred tank](#). *AIChE J* 63, 3610–3623.